# Optimal Periodic Variable Switching PWM for Harmonic Performance Enhancement in Grid-Connected Voltage Source Converters

Wu, Yang; Xu, Junzhong; Soeiro, Thiago B.; Stecca, Marco; Bauer, Pavol

**DOI**
10.1109/TPEL.2022.3141268

**Publication date**
2022

**Document Version**
Final published version

**Published in**
IEEE Transactions on Power Electronics

# Optimal Periodic Variable Switching PWM for Harmonic Performance Enhancement in Grid-Connected Voltage Source Converters

Yang Wu, *Student Member, IEEE*, Junzhong Xu, *Member, IEEE*, Thiago Batista Soeiro, *Senior Member, IEEE*, Marco Stecca, *Student Member, IEEE*, and Pavol Bauer, *Senior Member, IEEE*

***Abstract*—Variable switching frequency PWM (VSFPWM) modulation can be advantageously implemented in industrial applications, such as renewable energy, motor drives, and uninterrupted power supply (UPS) systems, to reduce the injected current harmonic amplitudes, to suppress audible noise, and to improve semiconductor power efficiency. In this article, the usage of periodic VSFPWM methods in a voltage source converter (VSC) is proposed, analyzed, and benchmarked in terms of harmonic spectrum spreading, following the IEEE-519 current harmonic standard for the connection to the distribution grid. Particular attention is paid to the influence of VSFPWM on the ac filter design. First, the analytical model of the voltage harmonic spectrum generated by a three-phase three-wire two-level VSC implementing several periodic VSFPWM methods is derived. Subsequently, a design guideline for the commonly used *LCL* filter in the grid-tied VSC application is proposed, which minimizes the size requirement of the necessary components. The voltage spectrum models of the proposed VSFPWM method and the optimal switching profiles are verified by MATLAB/Simulink simulations and a 5-kW three-phase two-level VSC hardware demonstrator. The study shows that the ac filter power density for the studied VSFPWM methods can be greatly increased when compared with the conventional and widely employed constant switching frequency continuous PWM strategies.**

***Index Terms*—Filter design, optimal design, spectrum model, variable switching frequency PWM (VSFPWM).**

## NOMENCLATURE

| | |
|---|---|
| $i_{\rm c}$, $i_{\rm g}$ | Converter-/grid-side phase current. |
| $V_{\rm ac}$, $v_{\rm ac}$ | AC source (grid) phase voltage. |
| $V_{\rm c}$, $v_{\rm c}$ | Converter output phase voltage. |
| $V_{\rm dc}$ | DC bus voltage. |
| $M$ | Modulation depth. |
| $J_{\rm n}(x)$ | Bessel function of the first kind. |
| $L_{\rm c}$, $L_{\rm g}$, $L_{\rm T}$ | Converter-/grid-side/total inductance. |
| $L_{\rm T}$ | *LCL* filter total inductance. |
| $C_{\rm f}$ | *LCL* filter capacitance. |
| $\omega_{\rm c}$, $\omega_{\rm o}$, $f_{\rm c}$, $f_{\rm o}$ | Carrier and reference frequency. |
| $\theta_{\rm c}$, $\theta_{\rm o}$ | Phase of carrier and reference signal. |
| $f_{\rm c0}$ | Centered switching (carrier) frequency. |
| $f_{\rm res}$ | *LCL* filter resonance frequency. |
| $f_{\rm m}$ | Frequency of periodic switching profile. |
| $\omega_{\rm b}$, $f_{\rm b}$ | Switching frequency variation band. |
| $\omega_{\rm crit}$, $f_{\rm crit}$ | Critical harmonic frequency. |
| $V_{\rm crit}$, $I_{\rm crit}$, $f_{\rm crit}$ | Critical harmonic voltage/current. |

Manuscript received August 14, 2021; revised November 11, 2021; accepted December 31, 2021. Date of publication January 7, 2022; date of current version February 18, 2022. This work was supported by the European H2020 Research and Innovation Program, ECSEL Joint Undertaking, and National Funding Authorities from eight participating countries, such as Austria, Finland, Germany, including the Free States of Saxony and Thuringia, Hungary, The Netherlands, Slovakia, Spain, and Switzerland under Grant 826417. Recommended for publication by Associate Editor B. (GAE) P. McGrath. *(Corresponding author: Junzhong Xu.)*

Yang Wu, Thiago Batista Soeiro, Marco Stecca, and Pavol Bauer are with the DCE&S Group, Department of Electrical Sustainable Energy, Delft University of Technology, 2628 CD Delft, The Netherlands (e-mail: Y.Wu-6@tudelft.nl; T.BatistaSoeiro@tudelft.nl; m.stecca@tudelft.nl; P.Bauer@tudelft.nl).

Junzhong Xu is with the Department of Electrical Engineering, Shanghai Jiao Tong University, Shanghai 200240, China, and also with the Key Laboratory of Control of Power Transmission and Conversion, Ministry of Education, Shanghai 200240, China (e-mail: junzhongxu@sjtu.edu.cn).

Color versions of one or more figures in this article are available at https://doi.org/10.1109/TPEL.2022.3141268.

Digital Object Identifier 10.1109/TPEL.2022.3141268

## I. INTRODUCTION

DUE to the rapid development of renewable technology and wider adoption of electric vehicles, the pursuit of compact and efficient grid-tied power electronic converters is becoming increasingly important for photovoltaic and wind power generation, and battery fast-charging stations. Pulsewidth-modulation (PWM)-based voltage source converters (VSCs) are widely employed as grid-tied converters because of their robustness and simplicity [1]. Correspondingly, *LCL* filters are adopted to mitigate the current harmonics generated by the PWM-based VSCs. Typically, the *LCL* filter is one of the bulkiest and heaviest parts in the high-power converter system. Hence, considerable research efforts in physical design and circuit topology have been devoted, aiming at reducing the filter size and weight. It is recognizable that the design of a smaller inductor is possible if the application requirements can be fullfilled with the need of less magnetic energy storage, e.g., by reducing the need of inductance value [2], [3]. Conventional approaches for reducing the harmonic generated by the VSC, and therefore the required filtering inductance, consist on increasing the switching frequency, adopting interleaved or multilevel converter topologies, and implementing specific modulations [4]–[9].

Variable switching frequency PWM (VSFPWM), for instance, is an interesting strategy to be implemented in VSCs because of its effectiveness in improving the switching loss, current ripple, Electromagnetic interference (EMI), and, above all,

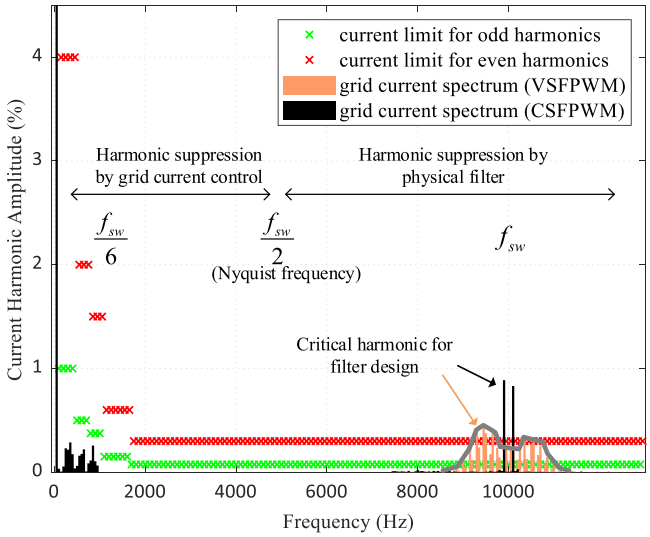


Fig. 1. IEEE-519 harmonic current standard and typical grid current harmonic spectrum with CSFPWM and VSFPWM.

its simple digital implementation [10]–[15]. More importantly, the spread spectrum caused by VSFPWM can also benefit the filter design for the VSC. However, there is lack of research efforts about this concept at present. The filter used for grid-tied converter must be well-designed to comply with the grid connection standard, in particularly the harmonic current standards such as IEEE-519-2014 [4]. As presented in Fig. 1, the VSFPWM method spreads out the converter output voltage spectrum, thus giving a similarly wide harmonic spectrum with lower amplitudes for the grid current compared with the normally adopted constant switching frequency PWM (CSFPWM), when an ac filter is applied. The magnitude of the critical harmonic for the filter design is significantly reduced by VSFPWM. In other words, the filtering requirement can be alternatively lowered with the VSFPWM while maintaining the same level of critical current harmonic presented by the CSFPWM. Therefore, the compact design of the *LCL* filter can be realized by the VSFPWM, leading to lower loss and weight in the filter, which can consequently improve the system efficiency and power density.

VSFPWM strategies can be categorized into two types: Random (or chaotic) and periodic switching frequency profiles. From the perspective of shaping the spectra of the PWM output voltage for filter design, the periodic patterns are preferred, since random profiles do not provide a tight control on the spectrum band [16]–[18]. The critical harmonic for the filter design is found to be closely correlated with the band of the spectrum induced by the periodic VSFPWM. Hence, the *LCL* filter can be designed in consideration of not only normal design criteria but also the profile of the periodic VSFPWM. Such a design requires the accurate voltage spectrum model of the three-phase PWM converter. The work in [17], [18] first studied the band of the spectrum induced by the periodic switching frequency profile in a PWM converter but did not provide further description of the spectrum contents. In [19], the spectrum model was presented in complex domain for dc/dc PWM converters with the consideration of the sinusoidal switching profile only. Recently, Li *et al.* [16] derived the analytical spectrum model for three-phase PWM converter based on the PWM output voltage expressions described by [20]. However, the derived model only applies to sinusoidal switching profile and is not valid for generic periodic switching profiles which include several harmonics instead of a single sinusoid.

The research on the *LCL* filter design with VSFPWM is very limited in the literature. Only the restraint of current ripple on the filter inductance [21], [22] or the basic requirement associated with the *LCL* filter resonance are considered [4], [23]. By contrast, this article investigates the influence of the VSFPWM following periodic switching frequency profiles on the design of the *LCL* filter of a three-phase, three-wire, two-level VSC which complies to the grid harmonic IEEE-519-2014 standard, illustrated in Fig. 1. The changing frequency profiles considered here are based on conventional waveform shapes, i.e., triangle and sinusoidal waveforms [17]–[19], due to their simple implementation in microcontrollers and straightforward identification of the critical current harmonic for the ac filter design. Therefore, the optimal periodic VSFPWM profile is identified in this article and a guideline for the *LCL* filter design is proposed, which maximizes the VSC power density.

The research contributions of this article are as follows.

1) The derivation of the PWM converter voltage spectrum model for the generic periodic VSFPWM profiles.
2) A straightforward design guideline for the *LCL* filter of a grid-tied VSC implementing a periodic VSFPWM profile which substantially reduce the ac filter requirement while maintaining the current total harmonic distortion (THD) and power efficiency which are achieved by the equivalent CSFPWM strategy.
3) The benchmaking and insights gained on the attained *LCL* filter performance in harmonic attenuation for grid compliance for several periodic profile VSFPWM and standard CSFPWM strategies.

The rest of this article is organized as follows. Section II presents the derivation of the time-domain model of the two-level VSC output voltage. Section III describes the design guidelines of the optimal periodic VSFPWM profile. Section IV discusses the simulation and experimental results verifying the developed analytical models and proposed *LCL* filter design. Finally, Section V concludes this article.

## II. Converter Voltage Spectrum Model

### A. Spectrum Model for CSFPWM

To simplify the analysis and model derivations, the sinusoidal-PWM (SPWM) is presented in this section. These mathematical derivations built based on the SPWM can be extended to other continuous PWM methods, e.g., THIPWM and SVPWM [20], [24], [25], which are preferably implemented in practical systems because of their higher dc bus voltage utilization. As depicted in Fig. 2, the converter output phase voltage $V_c$ of the three-phase, two-level converter is determined by the switching states of the semiconductor devices, which are directed by the intersections between the sinusoidal reference and triangular carrier signals, as illustrated in Fig. 3. According to the double

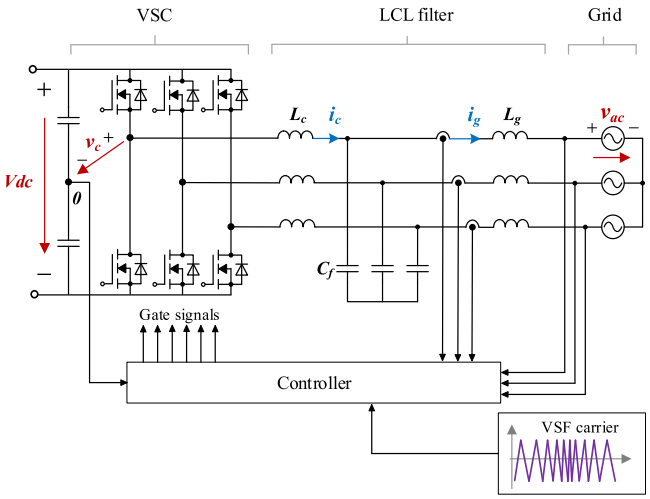


Fig. 2. Grid-tied VSC with *LCL* filter adopting VSFPWM.

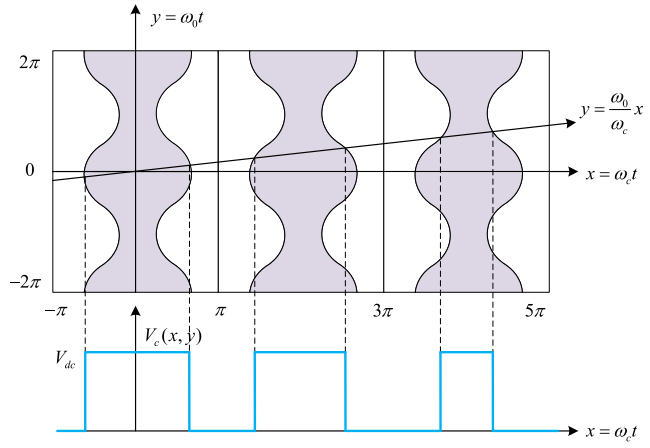


Fig. 3. Triangular carrier-based CSFPWM (natural sampling).

Fourier analysis (DFA) [20], the output phase voltage $V_c(x,y)$ is the function of two independent variables as expressed by (1), shown at the bottom of this page. In (1), $m$ and $n$ are multiples of the carrier and reference signal frequencies while $A_{\rm mn}$ and $B_{\rm mn}$ are the resultant coefficients of the DFA. The first term $A_{00}$ shown in (1) represents the dc offset, which is zero for the converter circuit shown in Fig. 2. The first summation term is the base-band harmonic components and the second summation term represents the carrier harmonic components. The last one represents the side-band harmonic components. The two variables $x$ and $y$ represent the phases of the carrier and reference signals under the constant carrier frequency modulation, respectively, which are expressed as

$$\begin{cases} x(t) = \omega_c t + \theta_c \\ y(t) = \omega_o t + \theta_o \end{cases} \tag{3}$$

where $\omega_c$ and $\omega_o$ are the angular frequencies for the carrier and reference signals (switching and fundamental frequencies), respectively, and $\theta_c$ and $\theta_o$ are the phases for the carrier and reference signals. The VSC output voltage with CSFPWM under the symmetrical regular sampling can be generally expressed as (2), shown at the bottom of this page in time-domain, with the complex-form coefficients derived by using the double-integral

$$\begin{aligned} C_{\rm mn} &= A_{\rm mn} + jB_{\rm mn} \\ &= \frac{1}{2\pi^2}\int_{-\pi}^{\pi}\int_{-\pi}^{\pi} V_c(x,y)e^{j(mx+ny)}{\rm d}x{\rm d}y. \end{aligned} \tag{4}$$

Therein $J_{\rm n}(x)$ is the Bessel function of the first kind, and $M$ is the modulation depth. $M$ is defined as $2V_{\rm ac}/V_{\rm dc}$ and $V_{\rm ac}$ and $V_{\rm dc}$ are the magnitude of the ac phase voltage and dc bus voltage, respectively [20].

$$V_c(x,y) = \frac{A_{00}}{2} + \underbrace{\sum_{n=1}^{\infty}(A_{0n}\cos ny + B_{0n}\sin ny)}_{\text{Fundemental component \& baseband harmonics}} + \underbrace{\sum_{m=1}^{\infty}(A_{m0}\cos mx + B_{m0}\sin mx)}_{\text{Carrier harmonics}}$$
$$+ \underbrace{\sum_{m=1}^{\infty}\sum_{\substack{n=-\infty \\ n\neq 0}}^{\infty}[A_{mn}\cos(mx+ny) + B_{mn}sin(mx+ny)]}_{\text{Sideband harmonics}} \tag{1}$$

$$\begin{aligned} V_{\rm c}(t) &= \frac{2V_{\rm dc}}{\pi}\sum_{n=1}^{\infty}\frac{J_{\rm n}(n\frac{\omega_{\rm o}}{\omega_{\rm c}}\frac{\pi}{2}M)}{(n\frac{\omega_{\rm o}}{\omega_{\rm c}})}\sin\left[n\left(1+\frac{\omega_{\rm o}}{\omega_{\rm c}}\right)\frac{\pi}{2}\right]\cos n(\omega_{\rm o}t+\theta_{\rm o}) + \frac{2V_{\rm dc}}{\pi}\sum_{m=1}^{\infty}\frac{J_0(m\frac{\pi}{2}M)}{m}\sin\left(m\frac{\pi}{2}\right)\cos[m(\omega_{\rm c}t+\theta_{\rm c})] \\ &+ \frac{2V_{\rm dc}}{\pi}\sum_{m=1}^{\infty}\sum_{\substack{n=-\infty \\ n\neq 0}}^{\infty}\frac{J_{\rm n}[(m+n\frac{\omega_{\rm o}}{\omega_{\rm c}})\frac{\pi M}{2}]}{m+n\frac{\omega_{\rm o}}{\omega_{\rm c}}}\sin[(m+n\frac{\omega_{\rm o}}{\omega_{\rm c}}+n)\frac{\pi}{2}]\cos[m(\omega_{\rm c}t+\theta_{\rm c})+n(\omega_{\rm o}t+\theta_{\rm o})] \\ &= \Re\left(\sum_{m=0}^{\infty}\sum_{n=-\infty}^{\infty}A_{\rm mn}\cdot e^{{\rm j}({\rm m}(\omega_{\rm c}{\rm t}+\theta_{\rm c})+{\rm n}(\omega_{\rm o}{\rm t}+\theta_{\rm o})))}\right) = \Re\left(\sum_{m=0}^{\infty}\sum_{n=-\infty}^{\infty}A_{mn}\cdot e^{{\rm j}({\rm mx}+{\rm ny})}\right) \end{aligned} \tag{2}$$

### B. Spectrum Model for Periodic VSFPWM

When periodic VSFPWM is applied, the phases of the two signals are modified as

$$\begin{cases} x(t) = \int_0^t \omega_{\rm c}(\tau){\rm d}\tau + \theta_{\rm c} \\ y(t) = \omega_{\rm o} t + \theta_{\rm o}. \end{cases} \tag{5}$$

The spectrum model, hence, becomes more complicated and very difficult to be directly derived with DFA because of the nonlinearity caused by the periodic time-varying variable $\omega_{\rm c}(t)$ appearing in the carrier angular frequency $x(t)$. Tripple Fourier analysis is also not applicable since variables $x(t)$ and $\omega_{\rm c}(t)$ are intercoupled and not linear. To derive the spectrum expression, some assumptions are adopted in this work to approximate the derived voltage expression.

1) The ratio between the centered switching frequency and the fundamental frequency $\omega_{\rm c0}/\omega_{\rm o}$ should be large enough, where the centered angular frequency $\omega_{\rm c0}$ is the average of $\omega_{\rm c}(t)$ during its period.
2) The variation band of the switching frequency $\omega_{\rm b}$ (or $f_{\rm b}$), which is half of the peak-to-peak variation of the switching profile, should be relatively small compared to the centered frequency $\omega_{\rm c0}$.

These two assumptions guarantee that the influence of the varying switching frequency on the coefficients presented in (2) can be negligible and hence the forms of these coefficients remain unchanged in the following mathematical derivations, except that $\omega_{\rm c}$ is replaced by $\omega_{\rm c0}$. A generic periodic switching frequency $f_{\rm c}(t)$ can be expanded into the following Fourier series:

$$\begin{aligned} f_{\rm c}(t) &= \frac{a_0}{2} + \sum_{k=1}^{\infty} a_{\rm k}\cos(2\pi k f_{\rm m} t) + b_{\rm k}\sin(2\pi k f_{\rm m} t) \\ &= f_{\rm c0} + \sum_{k=1}^{\infty} C_k \sin(2\pi k f_{\rm m} t + \theta_{\rm k}) \end{aligned} \tag{6}$$

where $f_{c0}$ is the centered switching frequency and $f_m$ is the frequency of the periodic switching profile. Substituting (5) and (6) into the phasor form presented in (4), and assuming that the initial phases of the carrier and reference signals are zero ($\theta_{\rm c}$, $\theta_{\rm o}$=0), then the expression of the output voltage becomes

$$\begin{aligned} V_c(t) &= \Re\left(\sum_{m=0}^{\infty}\sum_{n=-\infty}^{\infty} A_{\rm mn}\cdot e^{{\rm j}2\pi({\rm m}\int_0^{\rm t} {\rm f_c}(\tau){\rm d}\tau + {\rm nf_o t})}\right) \\ &= \Re\Bigg(\sum_{m=0}^{\infty}\sum_{n=-\infty}^{\infty}\{A_{mn}\cdot e^{{\rm j}(2\pi({\rm mf_{c0}+nf_o})t+\varphi_{\rm m})} \\ &\quad \cdot \underbrace{\prod_{k=1}^{\infty} e^{-{\rm j}\frac{{\rm mC_k}}{{\rm kf_m}}\cos(2\pi {\rm kf_m t}+\theta_{\rm k})}\}}_{\text{rear term due to VSFPWM}}\Bigg) \end{aligned} \tag{7}$$

where

$$\varphi_{\rm m} = \sum_{k=1}^{\infty} \frac{mC_{\rm k}\cos(\theta_{\rm k})}{kf_{\rm m}}. \tag{8}$$

In (7), the rear term is caused by the variation of the switching frequency. However, (7) is too complex and indirect to be used for calculation and thus requires a further simplification. By implementing Jacobi–Anger expansions [20], the expression for the output voltage can be simplified as

$$V_c(t) = \Re\left(\sum_{m=0}^{\infty}\sum_{n=-\infty}^{\infty}\sum_{l=-\infty}^{\infty} C_{\rm mnl}\cdot e^{{\rm j}2\pi({\rm mf_{c0}t+nf_o t+lf_m t})}\right) \tag{9}$$

where

$$C_{\rm mnl} = A_{\rm mn}e^{{\rm j}\varphi_{\rm m}}\cdot\left\{\sum_{\sum r_k\cdot k=l}(\prod_{k=1}^{\infty} h(m,k,r_k)\right\} \tag{10}$$

$$A_{\rm mn} = \frac{2V_{\rm dc}J_{\rm n}[(m+n\frac{\omega_{\rm o}}{\omega_{\rm c0}})\frac{\pi M}{2}]}{\pi(m+n\frac{\omega_{\rm o}}{\omega_{\rm c0}})}\sin\left[\left(m+n\frac{\omega_{\rm o}}{\omega_{\rm c0}}+n\right)\frac{\pi}{2}\right] \tag{11}$$

$$h(m,k,r) = J_{\rm r}(\frac{mC_{\rm k}}{kf_{\rm m}})\cdot e^{{\rm j}({\rm r}(\theta_{\rm k}-\pi/2))}. \tag{12}$$

Since the phase of the reference signal $\theta_{\rm o}$ is equal to zero, expression (9) describes analytically the output voltage of phase A, i.e., $V_{\rm c}$ with the VSFPWM. The expressions for phases B and C can be derived accordingly by replacing $\theta_{\rm o}$ with $-2\pi/3$ and $2\pi/3$, respectively. It is noteworthy that the spectrum of the output voltage can be obtained based on (9) because of the triple summation series form, and phasor representation. It can be noted that the side-band harmonics are the resultant contributed by the integer variables $n$ and $l$, which represent the side-band caused by CSFPWM and VSFPWM, respectively.

It is noted that the triple summation series form presented in (9) is valid only when the aforementioned two assumptions are satisfied. The assumptions guarantee that the difference of the coefficient $A_{\rm mn}$ during the switching frequency variation is negligible and thus the coefficient can be calculated at the centered frequency $f_{\rm c0}$, as shown in (11), and remains unchanged regardless of the switching frequency. The coefficient $C_{\rm mnl}$ contains the magnitude and phase information of the spectrum. However, for each possible side-band $lf_{\rm m}$ caused by VSFPWM there are infinite groups of $r_{\rm k}$ and hence the calculation of (10) becomes cumbersome. Specially, if $f_{\rm c}(t)$ varies sinusoidally with the frequency $f_m$, the coefficient $C_{\rm mnl}$ is reduced to

$$C_{\rm mnl} = A_{\rm mn}J_{\rm l}(\frac{mC_1}{f_{\rm m}})\cdot e^{j(\varphi_{\rm m1}+l(\theta_1-\pi/2))} \tag{13}$$

which is simpler and more convenient to use. Although the developed analytical spectrum model is derived based on SPWM, the same derivation approach is also applicable to other modulation methods, e.g, THIPWM and SVPWM. From (7), the rear term due to VSFPWM implies that the influence of the VSFPWM is decoupled from the normal CSFPWM operation.

Therefore, (9)–(11) still hold for other modulations while (11) should be replaced with the coefficient $A_{\mathrm{mn}}$ derived based on the CSFPWM operation according to the modulation adopted. The expression of $A_{\mathrm{mn}}$ for THIPWM and SVPWM can be found in [20], which is rather complicated and will not be presented in this article due to space limitations.

### C. DM and CM Harmonic Spectrum

In a three-phase three-wire VSC system, as the one shown in Fig. 2, due to the intrinsic high impedance for the generated zero sequence voltage components, only the differential-mode (DM) currents are considered to flow into the circuit for the spectrum of interest defined by the IEEE-519-2014 guidelines. Therefore, the circulating common-mode (CM) current components in both the converter- and grid-side currents are neglected regardless of the existence of CM components in the converter-generated output voltage. Based on this, for the purpose of the *LCL* filter design in a three-wire system, (10) should be used while only considering the DM components in the converter output voltage. This can be realized by separating the CM components from the original voltage spectrum. In other words, the use of (10) should neglect the terms with $n$ equals to zero and the triple multiples. Besides, for practical use of (10) to calculate the voltage harmonic at a specific harmonic order, some simplifications can be adopted to reduce the calculation time with adequate accuracy. Fig. 4 describes the procedures for the practical calculation of the specified voltage harmonic. Usually the first ten terms in the Fourier series expansion of the periodic waveform can give a satisfactory approximation [16]. The same approximation also holds for the Jacobi–Anger expansion because of the rapid roll-off of the Bessel function magnitudes [20]. Hence, the maximum value for both $r$ and $k$ shown in Fig. 4 is taken as 10.

To validate the correctness of the derived model without losing generality, the voltage spectrum generated by the analytical model is compared with the circuit simulation results under SPWM, THIPWM, and SVPWM [20]. Fig. 5 shows the simulated voltage harmonic spectra compared with the analytically constructed spectrum calculated by (10) under sinusoidal and triangle variable frequency profiles in the three different modulation cases. The profiles are implemented with $f_{\mathrm{c0}}$ =24.05 kHz and $f_{\mathrm{b}}$ =1 kHz. The remaining system parameters can be found in Table I. Since only the first carrier band spectrum is typically concerned with the design of the *LCL* filter, only the first carrier band spectra are shown in Fig. 5. In each modulation case, the CM and DM voltage spectra of either simulation or analytical results are separated and compared, respectively. The results illustrate that (10) can predict the harmonic spectra of the VSC-generated voltage well, which match the simulated results with relatively good accuracy. The results depicted hence verify the correctness of the model as well as the proposed calculation algorithm.

### D. Applicability to Low Switching Frequency

The two assumptions mentioned in Section II-B require a relatively larger centered switching frequency and narrowed variation band of the variable switching frequency to guarantee a

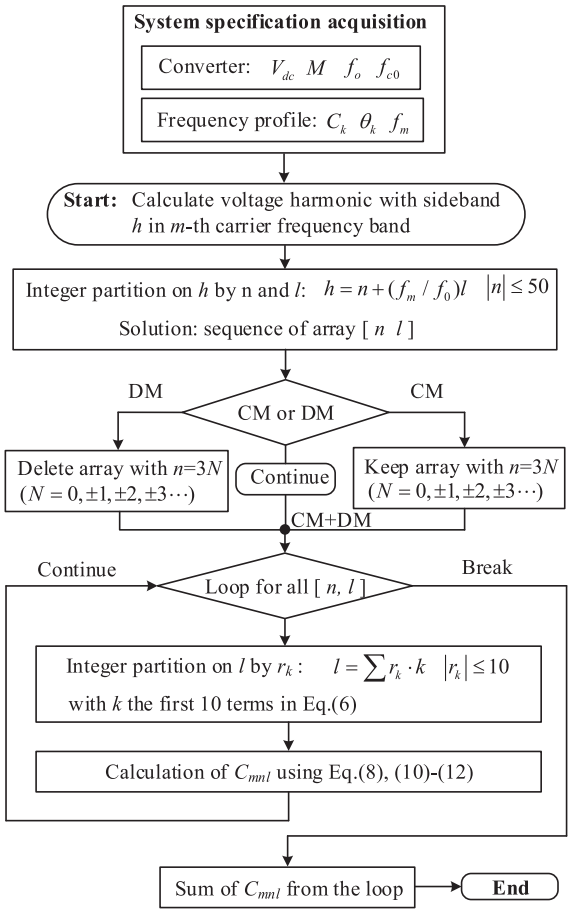


Fig. 4. Calculation algorithm of the VSC generated voltage spectrum.

TABLE I
SYSTEM PARAMETERS FOR SIMULATION AND EXPERIMENT

| PARAMETER | VALUE |
|---|---|
| **AC side** | |
| Voltage $V_{\mathrm{ac}}$ (rms) | 230 V |
| Fundamental frequency $f_o$ | 50 Hz |
| **Converter** | |
| Semiconductor | C3M0120090J |
| Blocking voltage $V_{\mathrm{B}}$ | 900 V |
| Drain current $I_{\mathrm{D}}$ | 14 A |
| Operating power | 2.2 kW |
| $V_{\mathrm{dc}}$ | 700 V |
| $C_{\mathrm{dc}}$ | 365 $\mu$F |
| $f_{\mathrm{c0}}$ | 24.05 kHz |
| $r_{\mathrm{f}}$ | 0.219 |
| **LCL Filter** | |
| Converter-side Inductance $L_{\mathrm{c}}$ | 370 $\mu$H |
| Grid-side Inductance $L_{\mathrm{g}}$ | 360 $\mu$H |
| Capacitance $C_{\mathrm{f}}$ | 5 $\mu$F |
| **Modulation** | SPWM, SVPWM<br>1/4 THIPWM |

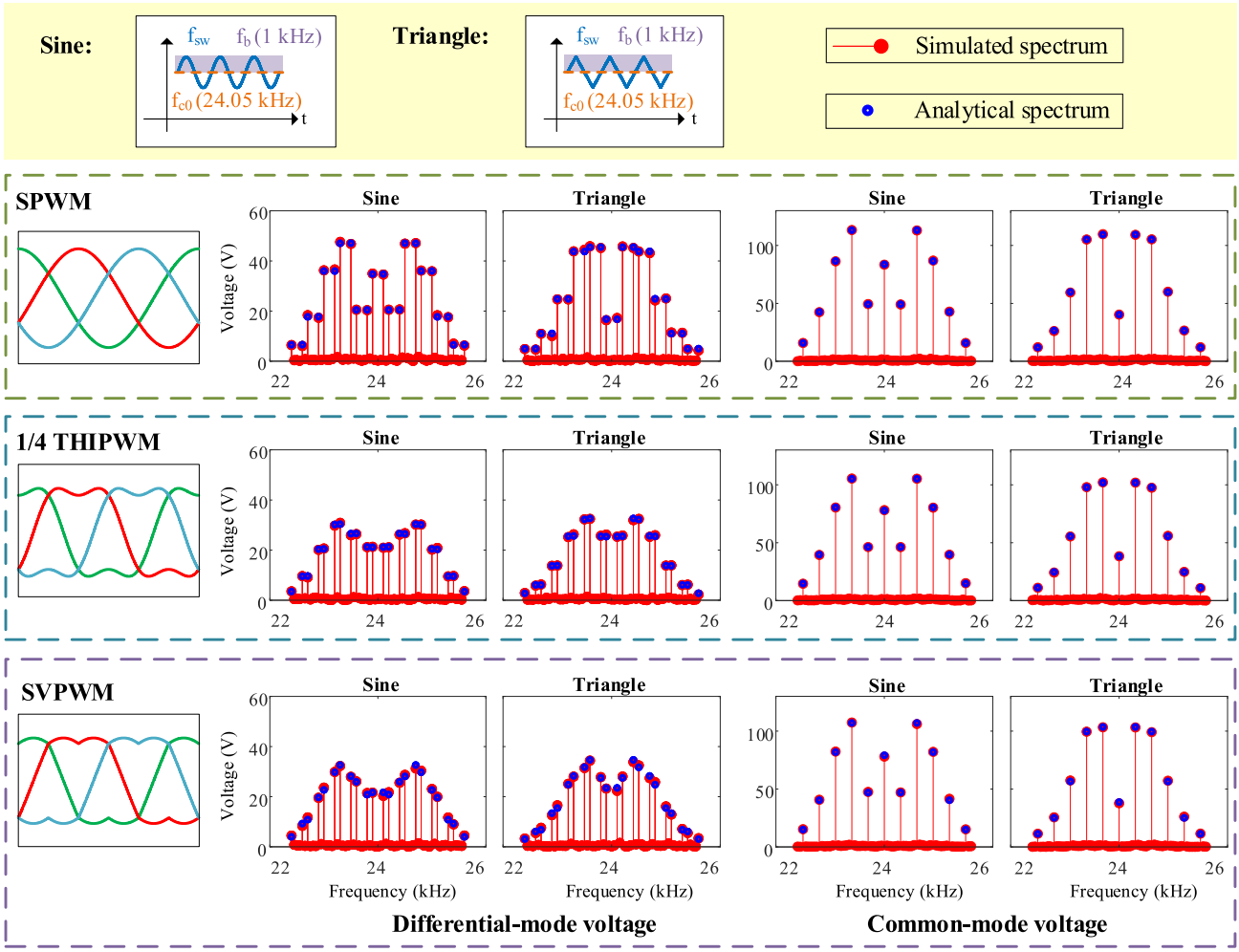


Fig. 5. Simulated and analytical converter output voltage spectrum under different modulations and frequency profiles.

reasonable approximation of the coefficient $A_{\mathrm{mn}}$ for VSFPWM as described in (11), where the following substitution is made:

$$n\frac{\omega_{\mathrm{o}}}{\omega_{\mathrm{c}}(t)} \Rightarrow n\frac{\omega_{\mathrm{o}}}{\omega_{\mathrm{c0}}}. \tag{14}$$

Still, it is necessary to quantify the applicable range of the centered switching frequency for the derived analytical spectrum model. In order to assess the accuracy of the model under different centered switching frequency other than 24.05 kHz, the voltage spectra given by the simulation and analytical results are compared for different cases of $f_{\mathrm{c0}}$, namely $f_{\mathrm{c0}} = 2$, 4, 8, 10, 12, and 16 kHz, respectively. The variation band $f_{\mathrm{b}}$ is always selected to be one-tenth the centered switching frequency to exhibit a fair comparison between different cases. Fig. 6 presents the root-mean-square error (RMSE) and the critical harmonic error between the simulated and analytical spectra under various modulation methods and periodic switching frequency profiles. The RMSE $\varepsilon_{\mathrm{RMSE}}$ is calculated by

$$\varepsilon_{\mathrm{RMSE}} = \sqrt{\frac{\sum_{k=1}^{N}(V_{\mathrm{simu}}(k) - V_{\mathrm{analy}}(k))^2}{N}} \tag{15}$$

where $V_{\mathrm{simu}}$ and $V_{\mathrm{analy}}$ represent the simulated and analytical voltage spectra and $N$ is the total number of harmonics to be calculated in the spectra. Undoubtedly, the voltage error arises with the lower centered switching frequency applied to the analytical spectrum model. Besides, the error is much greater under one-fourth THIPWM and SVPWM methods compared with SPWM. This is because the voltage harmonics spectra generated by 1/4 THIPWM and SVPWM under CSFPWM with regular sampling is more dependent on the term $n\omega_{\mathrm{o}}/\omega_{\mathrm{c0}}$ compared with the SPWM method [20]. Hence, the model becomes less accurate for 1/4 THIPWM and SVPWM under low centered switching frequency since (14) deviates from the assumptions. Finally, the error in the CM voltage components of the spectra is much smaller compared to the DM components. This is because the most CM harmonics in the spectra originate from the harmonic from CSFPWM, where the side-band $n = 0$. For those harmonics, (14) is always valid since the term becomes zero.

In summary, the derived analytical spectrum model becomes less accurate under low centered switching frequency due to the unavoidable symmetrical regular sampling process of the digital implementation of PWM in practice. However, the error is still

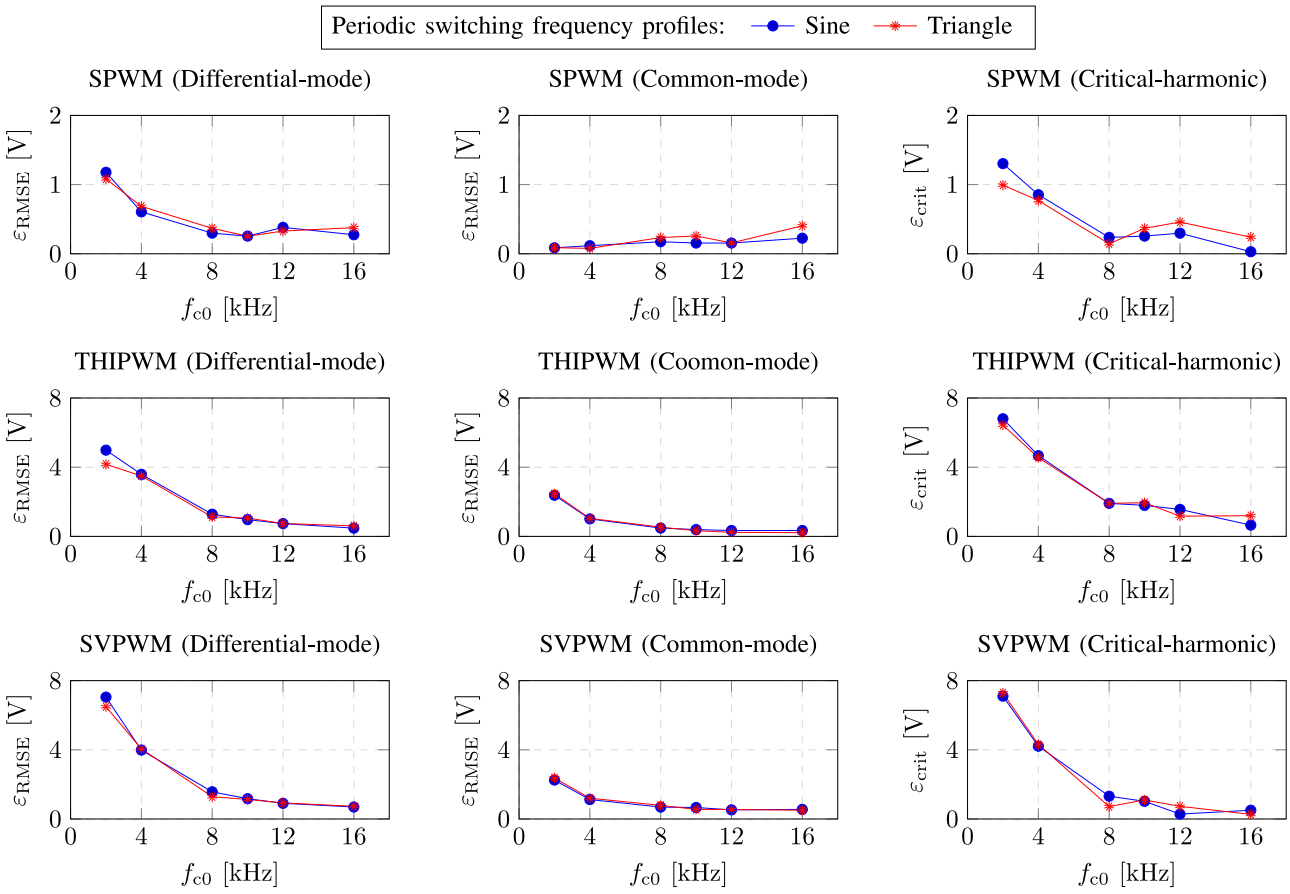


Fig. 6. Errors between the analytical and simulated results under lower centered switching frequency range.

acceptable if the centered switching frequency $f_{\mathrm{c0}}$ is selected to be larger than 4 kHz since the error is less than 4 V, which is relatively small (8%) compared to its critical harmonic magnitude. Usually a design margin of inductance will be considered for the inductor to deal with the inductance variation under high temperature and drop of permeability caused by current bias. Therefore, the proposed model can still be applicable to low centered switching frequency and the recommended range is $f_{\mathrm{c0}} \geqslant 4$ kHz.

## III. Design Guidelines for Periodic VSFPWM and *LCL* Filter

Some criteria and guidelines have been developed to assist the *LCL* filter design for the grid-connected VSC using the constant switching frequency PWM [1], [26]–[28]. The filter parameters are subsequently determined by the constraints defined by the design guidelines. The traditional filter design criteria or guidelines can also be applied with VSFPWM although some changes should be adopted due to the spread-spectrum characteristics. In this section, an *LCL* filter design guideline for VSFPWM is devised aiming to not only satisfy the grid harmonic standards, but also to keep the good performance of current THD and power efficiency close to which would be attained with the utilization of CSFPWM.

### A. Design Constraints for LCL Filter

Neglecting the internal resistance of the inductors and considering no passive damping in the filter, the transfer function from the converter output phase voltage $v_{\mathrm{c}}(s)$ to the grid-side current $i_{\mathrm{g}}(s)$ is expressed as follows:

$$\frac{i_{\mathrm{g}}(s)}{v_{\mathrm{c}}(s)} = \frac{1}{L_{\mathrm{c}}L_{\mathrm{g}}C_{\mathrm{f}}s(s^2+\omega_{\mathrm{res}}^2)} = \frac{\omega_{\mathrm{res}}^2}{L_{\mathrm{T}}s(s^2+\omega_{\mathrm{res}}^2)} \tag{16}$$

where $L_{\mathrm{c}}$ and $L_{\mathrm{g}}$ are the converter- and grid-side inductance of the *LCL* filter, respectively. $\omega_{\mathrm{res}}$ and $L_{\mathrm{T}}$ are the resonance frequency and the total inductance of the *LCL* filter, respectively, and expressed as

$$\omega_{\mathrm{res}} = \sqrt{\frac{L_{\mathrm{c}}+L_{\mathrm{g}}}{L_{\mathrm{c}}L_{\mathrm{g}}C_{\mathrm{f}}}} \tag{17}$$

$$L_{\mathrm{T}} = L_{\mathrm{c}} + L_{\mathrm{g}}. \tag{18}$$

Therefore, the attenuation from the voltage to the grid-side current can be represented by the magnitude of the transfer

function (16), as follows:

$$Att(\omega) = \left\| \frac{i_{\mathrm{g}}(j\omega)}{v_{\mathrm{c}}(j\omega)} \right\| = \frac{1}{L_{\mathrm{T}}} \cdot \frac{\omega_{\mathrm{res}}^2}{\omega \left| \omega^2 - \omega_{\mathrm{res}}^2 \right|}. \tag{19}$$

Equation (19) shows the attenuation capability of the *LCL* filter on the voltage harmonics. In grid-tied applications as a general guideline for harmonic compliance, the ac filters can be designed to meet the harmonic distortion limits established by the IEEE-519-2014, as depicted in Fig. 1. In medium- to high-switching frequency operated converters, the critical spectra content of the grid-side current should be attenuated to be less than the harmonic limit, namely 0.3% and 0.075% of the fundamental current for odd- and even-order harmonics, respectively, noted as $I_{\mathrm{IEEE519}}$ in this article. In constant frequency PWM operation, the output voltage only has few prominent side-band harmonics appearing in the vicinity of the first switching frequency band ($m$=1). Specifically for SPWM operation, by defining $m_{\mathrm{f}}$ as $\omega_{\mathrm{c}}/\omega_{\mathrm{o}}$, the critical frequency is found to be the $(m_{\mathrm{f}} - 2)$th order of the fundamental frequency since this voltage harmonic results in the largest current harmonic magnitude after the attenuation of the filter. $m_{\mathrm{f}}$ is usually selected to be odd integer so that the critical frequency becomes odd-order harmonic. Thereby, the stricter harmonic limit for the even harmonics can be avoided and the design of the minimum required inductance value is ensured.

The critical current harmonic should be attenuated to be below $I_{\mathrm{IEEE519}}$. In other words, the total inductance $L_{\mathrm{T}}$ should be selected to ensure that the critical current harmonic is below the limit set by the standard

$$Att_{\mathrm{req}} = \frac{I_{\mathrm{IEEE519}}}{V_{\mathrm{crit}}}. \tag{20}$$

By using (19) and (20), the minimum required total inductance of the *LCL* filter for satisfying the standard can be derived as

$$L_{\mathrm{T-req}} = \frac{\omega_{\mathrm{res}}^2 V_{\mathrm{crit}}}{\omega_{\mathrm{crit}} \left| \omega_{\mathrm{crit}}^2 - \omega_{\mathrm{res}}^2 \right| I_{\mathrm{IEEE519}}}. \tag{21}$$

From (21), the minimum required total inductance is proportional to the magnitude of the critical voltage harmonic $V_{\mathrm{crit}}$ and approximately inverse to the cubic of the critical frequency. Additionally, the minimum total inductance is also associated with the resonance frequency of the *LCL* filter. To avoid the instability caused by the filter resonance and to realize a stable grid-side current control, the resonance frequency of the *LCL* filter should be designed with regard to the so-called critical frequency [29], [30]. The resonance frequency should be larger than one-sixth of the switching frequency to attain the inherent stability without extra damping methods applied [31], [32]. In this work, the resonance-switching ratio $r_{\mathrm{f}} = f_{\mathrm{res}}/f_{\mathrm{c0}}$ is selected to be 0.219, as listed in Table I and remains fixed during the following designs developed in this article.

### B. Optimized Design of $f_{\mathrm{m}}$, $f_{\mathrm{b}}$, and $L_{\mathrm{T}}$

When VSFPWM is adopted, the voltage and consequently the current spectra content across the ac filter are spread differently depending on the switching profiles adopted. Therefore, the critical harmonic order $(m_{\mathrm{f}} - 2)$th derived for CSFPWM does not apply to VSFPWM due to the varied spectrum. Moreover, the critical frequency cannot be found straightforwardly from the nonintuitive spectrum. However, it is noteworthy that the critical frequency is closely associated with the applied switching profile. Fig. 7 depicts the critical frequency $f_{\mathrm{crit}}$ and switching frequency variation band $f_{\mathrm{b}}$ in the spectrum plot by using sinusoidal profile as an example. It is noted that $f_{\mathrm{crit}}$ is related to $f_{\mathrm{b}}$, and hence, the choice of $f_{\mathrm{b}}$ also influences the design of the total inductance $L_{\mathrm{T}}$ of the *LCL* filter. Besides, $V_{\mathrm{crit}}$ is not only associated with $f_{\mathrm{b}}$ but also with the periodic frequency $f_{\mathrm{m}}$. Therefore, the influence of the design variables $f_{\mathrm{m}}$ and $f_{\mathrm{b}}$ on $L_{\mathrm{T}}$ should be investigated before determining the total inductance value.

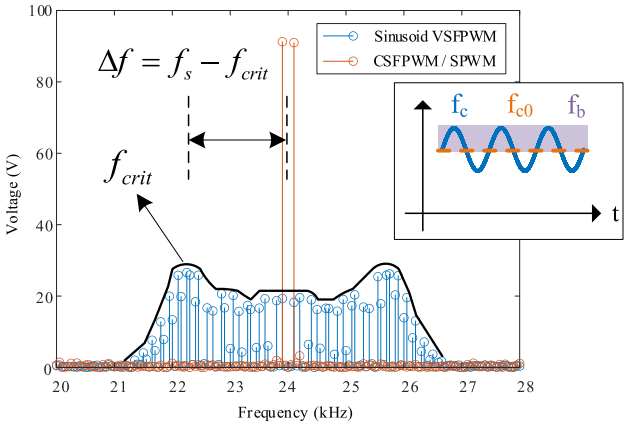


Fig. 7. Critical harmonic frequency and switching frequency variation band for sinusoidal VSFPWM and conventional CSFPWM.

Before the derivation of the relation between the critical frequency $f_{\mathrm{crit}}$ and $f_{\mathrm{b}}$, the periodic frequency $f_{\mathrm{m}}$ should be first determined. Fig. 8 presents the three-phase converter voltage spectra under $f_{\mathrm{m}}$ equal to different multiples of $f_{\mathrm{o}}$. Except the case of $f_{\mathrm{c0}} = 3f_{\mathrm{o}}$, the voltage spectra between three phases are not identical in magnitude for rest cases. Theoretically, when a single triangle carrier wave is used for the modulation of all three phases, $f_{\mathrm{m}}$ should be chosen as triple multiples of the fundamental frequency $f_{\mathrm{o}}$ to ensure that the harmonic spectra of the VSC output voltages remain symmetrical between three phases. That is

$$f_{\mathrm{m}} = 3kf_{\mathrm{o}} \tag{22}$$

where $k$ is a non-zero positive integer value. Similar to the CSFPWM case, the side-band harmonics including the critical harmonic are expected to be placed at an odd harmonic order. If $m_{\mathrm{f}}$ is defined as $f_{\mathrm{c0}}/f_{\mathrm{o}}$ for the VSFPWM operation, then the requirement can be expressed as

$$\begin{cases} nf_{\mathrm{o}} + lf_{\mathrm{m}} = (2N-1)f_{\mathrm{o}} & m_{\mathrm{f}} \text{ is even} \\ nf_{\mathrm{o}} + lf_{\mathrm{m}} = 2Nf_{\mathrm{o}} & m_{\mathrm{f}} \text{ is odd} \end{cases} \tag{23}$$

where $N$ is the arbitrary integer value. By using (22), (23) can be simplified as

$$\begin{cases} n + 3l \cdot k = 2N - 1 & m_{\mathrm{f}} \text{ is even} \\ n + 3l \cdot k = 2\tilde{}N & m_{\mathrm{f}} \text{ is odd.} \end{cases} \tag{24}$$

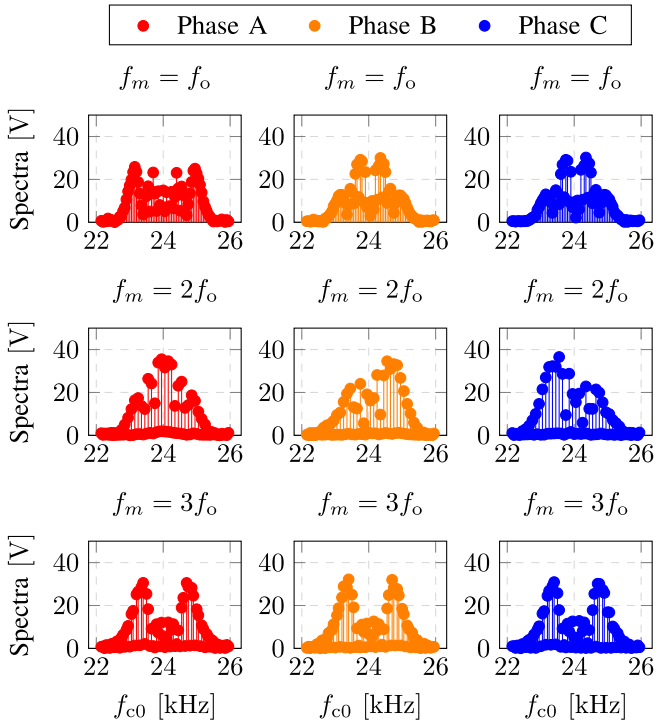


Fig. 8. Differential-mode spectra of the three phase voltages with SVPWM method and triangle periodic switching profile at $f_m$=$f_o$, $2f_o$, $3f_o$.

By analyzing the voltage spectrum with CSFPWM, it has been found that only even side-band harmonics appear in the spectrum, which means that $n$ is an even number. Therefore, the first argument where $m_f$ is eliminated because there exists no such integer $k$ satisfying the first condition for any values of $n$ and $l$. The second condition holds if $k$ is selected to be an even number. Hence, the periodic frequency $f_m$ of the switching frequency should satisfy

$$f_m = 6kf_o. \tag{25}$$

The critical frequency $f_{crit}$ is obtained by finding the most dominant harmonic by applying a normalized attenuation of the *LCL* filter to the spectrum of the output voltage. The expression of the normalized attenuation is given by

$$Att_{\mathrm{norm,LCL}}(\omega) = \frac{\omega_{res}^2}{\omega\,|\omega^2 - \omega_{res}^2|}. \tag{26}$$

Hence, the normalized critical harmonic current $I_{\mathrm{crit,norm}}$ can be found by

$$I_{\mathrm{crit,norm}} = max(|V_c(\omega)| \cdot Att_{\mathrm{norm,LCL}}(\omega)). \tag{27}$$

The critical voltage harmonic is expressed as

$$V_c(\omega) = \sum C_{mnl} \tag{28}$$

where $\omega$ satisfies

$$\omega = 2\pi(mf_{c0} + nf_o + lf_m). \tag{29}$$

In (29), the multiple of the carrier harmonic $m$ is selected to be 1 since the critical harmonic exists in the side bands of the first carrier harmonic. The critical voltage harmonic then is

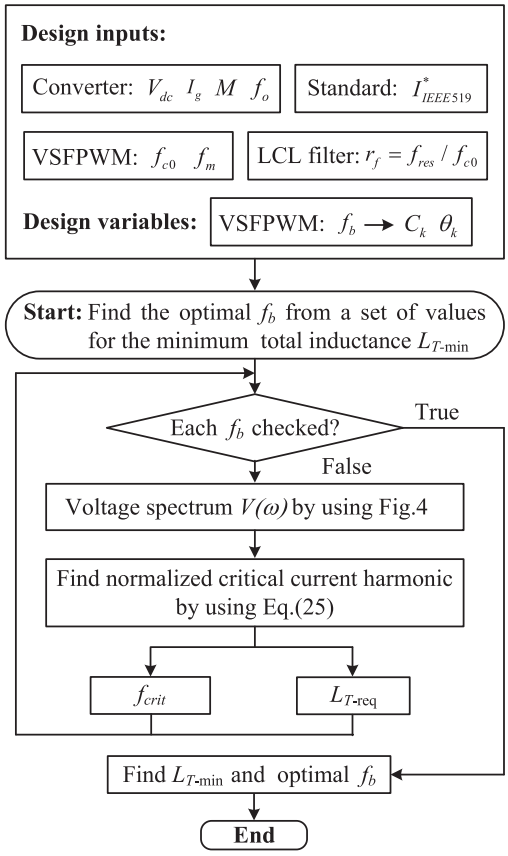


Fig. 9. Algorithm for optimal $f_b$ to achieve minimum total inductance $L_T$.

calculated according to the algorithm described in Fig. 4. Finally, the critical frequency $f_{\mathrm{crit}}$ hence can be found by retrieving the corresponding frequency from $I_{\mathrm{crit,norm}}$. As a result, the distance $\Delta f$ between the critical frequency $f_{\mathrm{crit}}$ and the centred switching frequency $f_{c0}$ is obtained. The required total inductance $L_{\mathrm{T-req}}$ can be subsequently derived by using (21).

In order to find the optimal $f_b$ and the consequent minimal $L_{\mathrm{T-req}}$, the algorithm shown in Fig. 9 has been proposed. For the certain modulation method and VSFPWM profile shape, the algorithm requires the converter specifications such as the rated grid voltage and current $V_g$ and $I_g$, the modulation index $M$, and the fundamental frequency $f_o$. Besides, $f_{c0}$ and $f_m$ of the VSFPWM, the current harmonic limit and the filter resonance frequency are also input to the algorithm. The algorithm finds the critical frequency and the associated required total inductance $L_{\mathrm{T-req}}$ for each $f_b$ from a wide range set of values. Finally, the minimum $L_{\mathrm{T-req}}$ can be found by traversing the whole range and the related $f_b$.

With the algorithm shown in Fig. 9, the relations between $f_b$ and $\Delta f$ are presented in Fig. 10. From Fig. 10, $\Delta f$ shows a different staircase quasi-linear relation with $f_b$ under the SPWM, 1/4 THIPWM, and SVPWM methods. Besides, the minimum required total inductance under various $f_b$ is also found by using the algorithm and presented in Fig. 11. Regardless of the modulation method, the required total inductance under the periodic switching profiles always drops with the initial increase of $f_b$ and then begins to increase from a certain value of $f_b$.

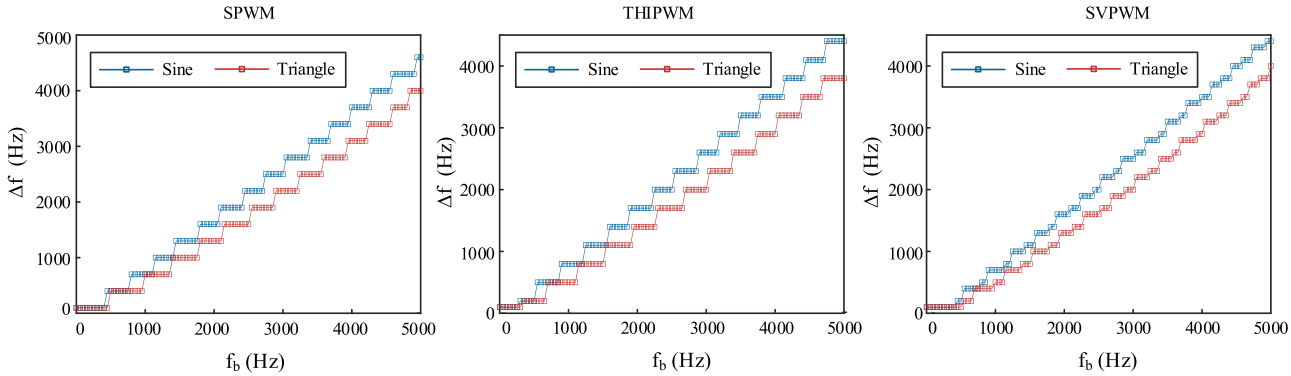


Fig. 10. Relation between $f_b$ and $\Delta f$ under various VSFPWM methods and frequency profiles.

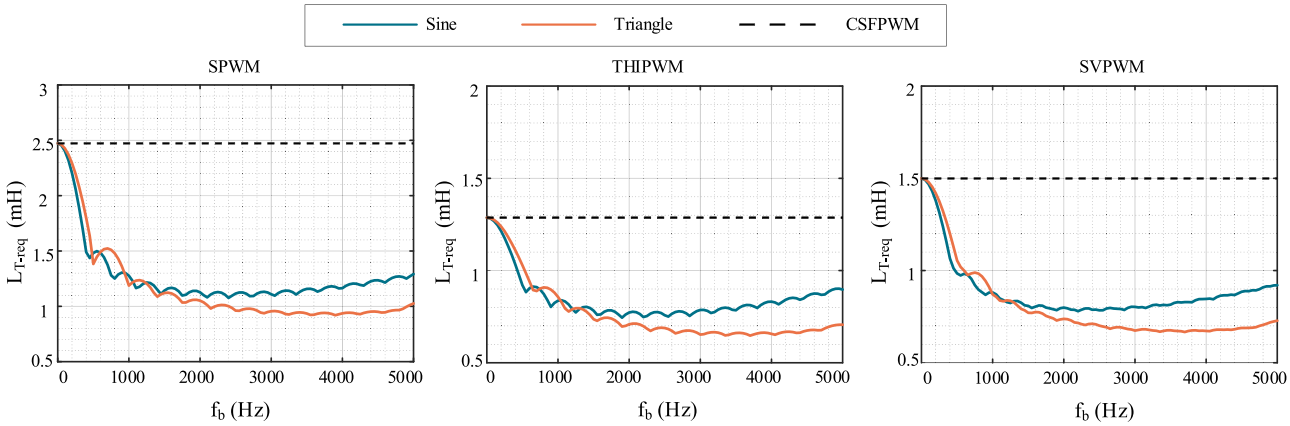


Fig. 11. Relation between the required total inductance $L_T$ and $f_b$ under various VSFPWM methods and frequency profiles.

TABLE II
DESIGNED OPTIMAL SWITCHING PROFILES

| VSFPWM switching Profile | $f_{\rm b}$ (Hz) | $L_{\rm T-req}$ ($\mu$H) |
|---|---|---|
| **SPWM** | | |
| CSFPWM | —— | 2560 |
| VSFPWM sinusoid profile | 2400 | 1115 |
| VSFPWM triangle profile | 3900 | 947 |
| **1/4 THIPWM** | | |
| CSFPWM | —— | 1330 |
| VSFPWM sinusoid profile | 1900 | 772 |
| VSFPWM triangle profile | 3700 | 667 |
| **SVPWM** | | |
| CSFPWM | —— | 1565 |
| VSFPWM sinusoid profile | 2200 | 810 |
| VSFPWM triangle profile | 3700 | 710 |

The optimal points giving the maximum inductance drop are summarized in Table II. Compared with the CSFPWM, the sinusoid and triangle VSFPWM profiles lead to a remarkable reduction of the required total inductance. Specifically, the triangle profile can result in a larger reduction compared with the sinusoid profile, which is around 50%–60% depending on the modulation method. Compared with SPWM, both SVPWM and 1/4 THIPWM methods require less total inductance $L_{\rm T-req}$, but also they feature similar inductance drop tendency.

### C. Selection of $L_c$, $L_g$, and $C_f$

As a constraint for the filter design, the maximum ac filter capacitance $C_{\rm f}$ is limited by the maximum allowable reactive power to be compensated by the VSC, which is consumed by this component at the point-of-coupling (PCC). This is important to limit the circulating reactive power, which could reduce the converter power efficiency, particularly at partial or low-load conditions. Hence, the filter capacitance should fulfil the requirement

$$C_{\rm f} < q \cdot \frac{S_{\rm N}}{3\omega_{\rm o} V_{\rm ac}^2} \tag{30}$$

where $S_{\rm N}$ is the rated power of the system and $q$ is ratio of the device fundamental reactive power and set to 5% in this article.

As aforementioned, $r_{\rm f}$, namely the ratio between the resonance and switching frequency, is set to be larger than 1/6 to achieve the stability of grid-side current control with the inherent damping under the continuous PWM methods adopted in this article [31], [32]. Hence, the extra active damping means can be avoided, which simplifies the potential controller. The converter-

and grid-side inductance will be determined subsequently after the value of the total inductance $L_T$ is selected based on (21). By combining (17) and (18), $L_c$ and $L_g$ are derived by

$$L_{\mathrm{c,g}} = \frac{L_{\mathrm{T}}}{2} \pm \sqrt{\frac{L_{\mathrm{T}}^2}{4} - \frac{L_{\mathrm{T}}}{\omega_{\mathrm{res}}^2 C_{\mathrm{f}}}} \tag{31}$$

where the total inductance satisfies

$$L_{\mathrm{T}} \geqslant \frac{4}{\omega_{\mathrm{res}}^2 C_{\mathrm{f}}}. \tag{32}$$

Besides, the upper limit of the total inductance is constrained by the maximum converter phase voltage and the rated grid-side current by considering the voltage drop of $L_{\mathrm{T}}$ [1].

$$L_{\mathrm{T}} \leqslant \frac{\sqrt{\frac{V_{\mathrm{dc}}^2}{6} - V_{\mathrm{ac}}^2}}{\omega_{\mathrm{o}} I_{\mathrm{g}}}. \tag{33}$$

Usually the larger value in (31) is selected for $L_c$ for the purpose of limiting the converter current ripple. The *LCL* filter parameters designed for the SVPWM operation with triangle VSFPWM profile are listed in Table I.

### D. Influence on the Switching Loss and Control

The semiconductor switching loss can be modeled as [33]

$$P_{\mathrm{sw}} = \frac{f_{\mathrm{c}} V_{\mathrm{dc}}}{2\pi V_{\mathrm{ref}}} \int_0^{2\pi} E_{\mathrm{on,off,rr}} \mathrm{d}\omega_{\mathrm{o}} t \tag{34}$$

where $V_{\mathrm{ref}}$ is the normalized dc voltage provided in datasheet. $E_{\mathrm{on,off,rr}}$ represents the switching energies and can be expressed as second-order polynomial function of the current

$$E_{\mathrm{on,off,rr}} = ai(t)^2 + bi(t) + c \tag{35}$$

$$i(t) = I\sin(\omega_{\mathrm{o}} t + \varphi). \tag{36}$$

Combine (6), (25), and (34)–(36), the switching loss model for the periodic VSFPWM becomes

$$\begin{aligned} P_{\mathrm{sw}} &= P_{\mathrm{sw0}} + \frac{V_{\mathrm{dc}}}{2\pi V_{\mathrm{ref}}} \sum_{k=1}^{\infty} \left( \int_0^{2\pi} \left( -\frac{aI^2\cos(2\omega_{\mathrm{o}} t + 2\varphi)}{2} \right.\right. \\ &\quad \left.\left. + bI\sin(\omega_{\mathrm{o}} t + \varphi) \right) + c + \frac{aI^2}{2} \right) \cdot C_{\mathrm{k}} \sin(6k\omega_{\mathrm{o}} t + \theta_{\mathrm{k}}) \mathrm{d}\omega_{\mathrm{o}} t) \\ &= P_{\mathrm{sw0}} \end{aligned} \tag{37}$$

where $P_{\mathrm{sw0}}$ is the switching loss under CSFPWM with the centered switching frequency $f_{\mathrm{c0}}$ and is expressed as

$$P_{\mathrm{sw0}} = \frac{f_{\mathrm{c0}} V_{\mathrm{dc}}}{2\pi V_{\mathrm{ref}}} \int_0^{2\pi} E_{\mathrm{on,off,rr}} \mathrm{d}\omega_{\mathrm{o}} t. \tag{38}$$

The second term in (37) becomes zero due to the orthognality between the integrated functions regardless the current phase angle $\varphi$. This implies this conclusion applies to all three phases of the PWM converter. Besides, (37) means that the proposed periodic PWM method does not cause extra semiconductor switching loss compared to CSFPWM and hence will not bring additional thermal stress on the semiconductor devices.

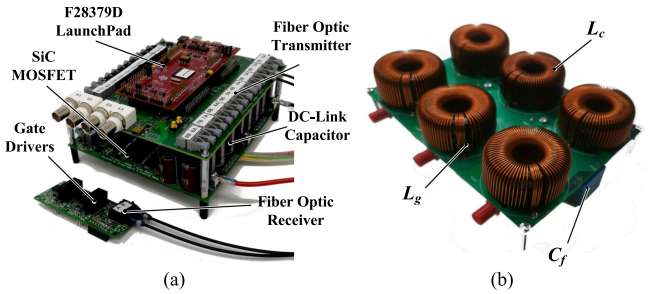


Fig. 12. Experimental setup. (a) VSC. (b) *LCL* filter.

Since the current harmonics are concerned in this article, the current controller for the PWM converter should be designed to be capable of rejecting the low-order harmonics below the Nyquist frequency ($f_c$/2) of the system. Therefore, minimum applicable centered switching frequency can be identified by setting the minimum possible Nyquist frequency to be greater than the mostly concerned low-order harmonic frequencies. In IEEE519 standard, for instance, the harmonics only count up to 35th order. Hence, we have

$$\frac{f_{\mathrm{c-min}}}{2} = \frac{f_{\mathrm{c}} - f_{\mathrm{b}}}{2} > 35 \cdot f_{\mathrm{o}}. \tag{39}$$

Based on [17], [18], $f_{\mathrm{b}}$ should satisfy

$$f_{\mathrm{b}} \leqslant \frac{f_{\mathrm{c0}} - 2f_{\mathrm{m}}}{3} \tag{40}$$

to avoid the overlapping of the spectra of the first and second carrier frequency regions. Substitute (25) into (29), and the minimum centered switching frequency can be found by

$$f_{\mathrm{c0}} > 99 f_{\mathrm{o}}. \tag{41}$$

Therefore, $f_{\mathrm{c0}}$ is greater than 5 kHz for our typical application. Combining the range $f_{\mathrm{c0}} \geqslant$4 kHz derived in Section II-D, $f_{\mathrm{c0}}$ is greater than 5 kHz for the considerations of both the low-order harmonics rejection capability for the potential current controller and applicability of the derived analytical spectrum model.

## IV. Simulation and Experimental Results

To validate the correctness of the spectrum models and the optimal switching profiles, both simulation and experimental tests are conducted and compared with various PWM methods on the studied three-phase, three-wire, two-level VSC depicted in Fig. 2. First, a MATLAB/Simulink-based simulation is carried out. Thereafter, the adopted periodic switching profiles are realized on a digital-controlled hardware platform with the DSP TMS320F28379D from Texas Instruments. The key specifications of the considered VSC are listed in Table I.

In order to further validate the correctness and feasibility of the proposed model, the switching profiles listed in Table II are experimentally realized in a 5-kW prototype based on the power electronic circuit shown in Fig. 2. This is shown in Fig. 12. Therein, for the power semiconductors, three hard-paralleled SMD packaged 900-V silicon carbide (SiC) MOSFETs are used per necessary active switch. For the rated power, only natural convection PCB-mounted heat sinks are necessary for the

thermal management of the devices junction temperatures. A 200-MHz dual core microcontroller unit (MCU) from Texas Instruments assembled in a LaunchPad development kit is used. A master PC is used to control the operating modes programmed in the MCU through a USB communication link, which is electrically isolated by a XDS100v2 debug probe. Additionally, to achieve a high CM rejection ratio and also for human safety reasons, the control and the power boards are interconnected through optical fiber links. For the implementation of the conventional d–q controller, all the necessary analog-to-digital conversions of the inverter required measurements, namely the ac converter- and grid-side terminal currents, and the ac grid voltages and dc terminal voltages, are performed in the power board using 10-MHz delta-sigma modulators. The measured data is transmitted to the available sigma–delta filter channels of the MCU through a 50 BMd fiber optic transmitter. The *LCL* filter board depicted in Fig. 12(b) is built with two toroidal-core inductors with 370 and 360 $\mu$H, respectively, which are measured with an impedance analyzer. A film capacitor of 5 $\mu$F is used as the ac filter capacitor. The component value selection was devised using the design guideline presented in Section III while considering the VSFPWM strategy employing 1/4 THIPWM and triangular frequency profile. As it will be shown in the following, this strategy leads to the smallest requirement of $L_T$ for the operational condition listed in Table I. In experiments, the three-phase, two-level converter is operated in the inverter mode operating at full power factor at PCC. All of the experimental waveforms and data used in this article are recorded by the oscilloscope YOKOGAYA DLM2054, and the current THD and power conversion efficiency of the converter are tested by the power analyzer YOKOGAYA WT500.

### A. Validation of Periodic VSFPWM Spectrum Model

The correctness of the analytical VSFPWM spectrum model has already been verified by comparing the simulated and analytical converter output voltage spectra, which is shown in Fig. 5. The nine different switching profiles listed in Table II are examined by both simulation and experiment. The simulation and experimental results with the measured waveform are shown in Figs. 14 and 15, respectively. Due to the limitation of the oscilloscope channels, only one-phase output current/voltage waveforms are recorded in the experiment. By using the fast Fourier-transform method on the converter-generated output voltage (or $v_c$), i.e., the purple waveform in Fig. 15, the generated output voltage's spectra from the experimental results are obtained and presented in Fig. 13, in comparison with the spectra constructed by the proposed spectrum model described in Section II.

It can be noted that the spectra from the experimental results match the analytical ones well in all PWM methods and periodic switching profiles. With the analysis on the spectra, the maximum discrepancy between the two spectra is 1.7 V, which is 0.5% of the fundamental voltage and hence can be regarded to be negligible from the design point of view. From the spectra shown in Fig. 13, it can be noted that the triangle profiles in fact exhibit a more evenly spread spectrum compared to the sinusoid profile. This finally results in a smaller critical voltage harmonic requirement to be filtered out. The difference of the magnitude between the critical voltage in the spectra is reflected by the difference of the required inductance shown in Fig. 11. By analyzing the critical voltages of the six shown spectra, it is found that the 1/4 THIPWM with the triangle profile ($f_{\rm b}$) results in the smallest magnitude of the critical voltage, which implies that the minimum value of the required inductance is obtained for this operating case. Besides, the magnitude of the critical voltages is found to be positively correlated to the required inductance values shown in Table II. Thereafter, it can be concluded that the analytical model of the periodic VSFPWM spectrum is verified to be correct based on the analysis from the simulation and experimental results.

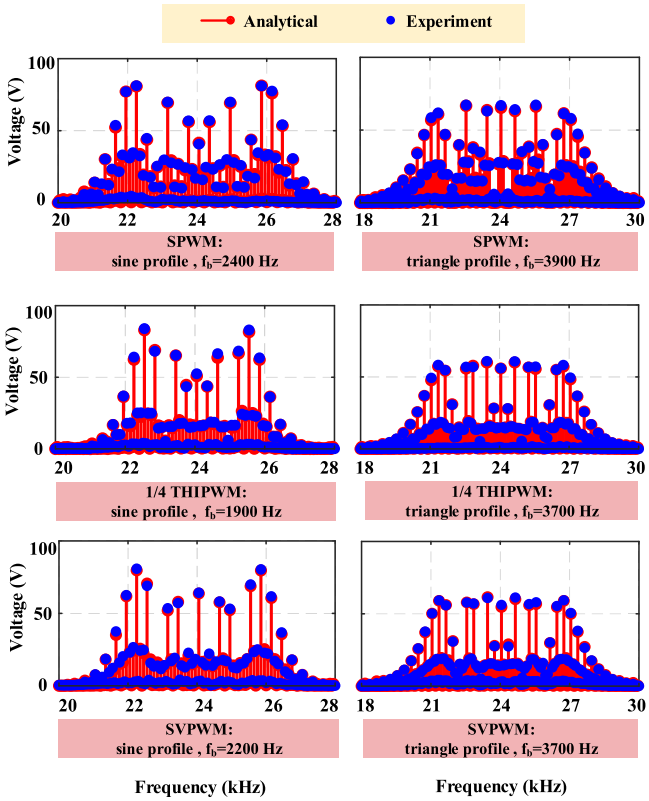


Fig. 13. Comparison between the analytical and experimental results of the converter output voltage spectra of the first carrier band under various switching profiles and PWM methods.

### B. Validation of the Optimal Switching Profile

Besides the validation of the VSFPWM spectrum model, the design of the optimal switching profile is also validated by the simulation and experimental tests. The parameters in Table I are used for both the simulations and experiments. Fig. 14 shows the simulation results of the converter output voltage $v_{\rm c}$, converter-side current $i_{\rm c}$, grid-side current $i_{\rm g}$, and the ac voltage $v_{\rm ac}$ under the nine designed switching profiles listed in Table II. The ac voltage $v_{\rm ac}$ has a peak value of 325 V while the grid-side current has a peak value of 4.3 A. It can be seen that the periodic switching profiles work well under

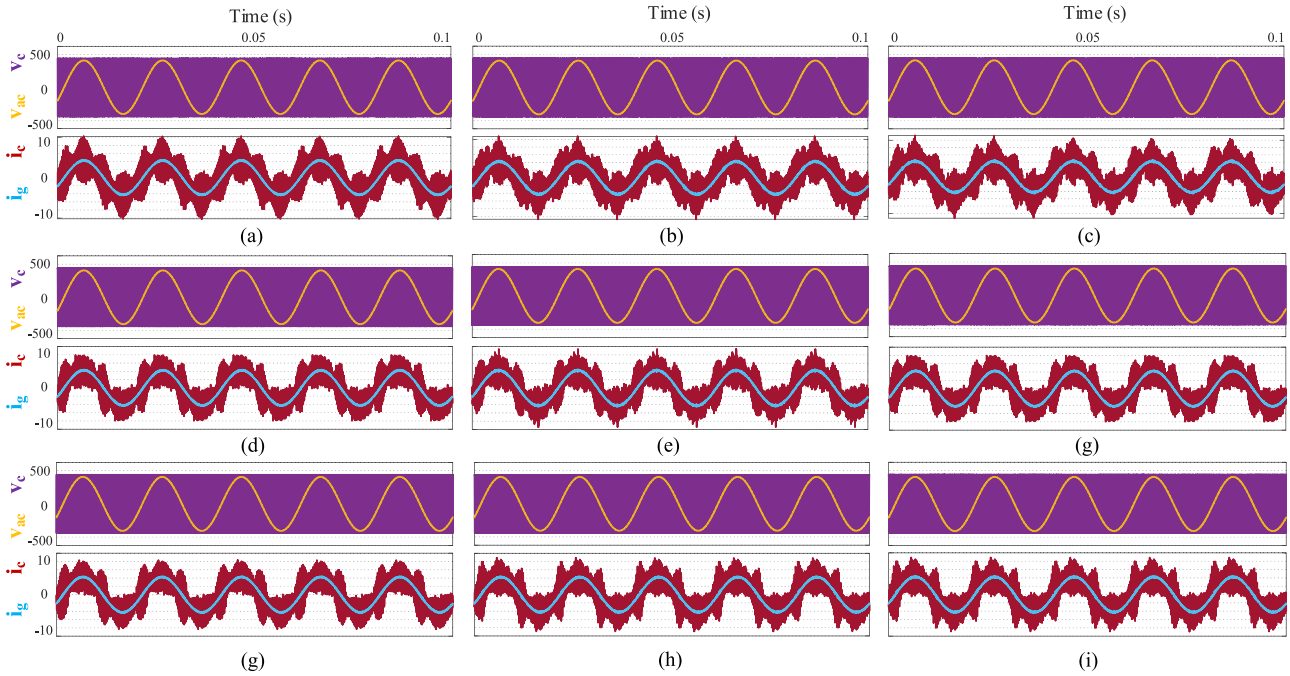


Fig. 14. Simulation results of the three-phase, three-wire, two-level converter under various switching profiles and PWM methods. (a) SPWM—constant switching frequency. (b) SPWM—sinusoid profile: $f_b$=2400 Hz. (c) SPWM—triangle profile: $f_b$=3900 Hz. (d) THIPWM—constant switching frequency. (e) THIPWM—sinusoid profile: $f_b$=1900 Hz. (f) THIPWM—triangle profile: $f_b$=3700 Hz. (g) SVPWM—constant switching frequency. (h) SVPWM—sinusoid profile: $f_b$=2200 Hz. (i) THIPWM—triangle profile: $f_b$=3700 Hz. Note that only one of the three phase waveforms is recorded.

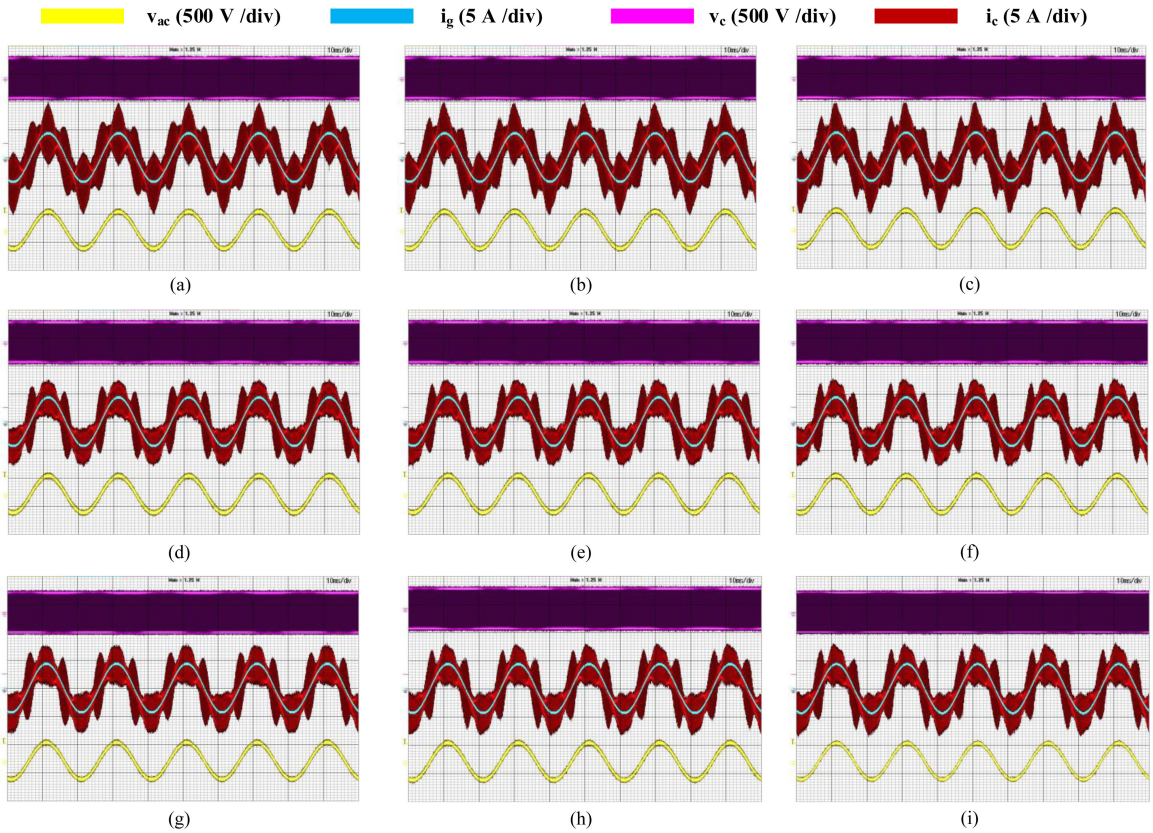


Fig. 15. Experimental results of the three-phase, three-wire, two-level converter under various switching profiles and PWM methods. (a) SPWM—constant switching frequency. (b) SPWM—sinusoid profile: $f_b$=2400 Hz. (c) SPWM—triangle profile: $f_b$=3900 Hz. (d) THIPWM—constant switching frequency. (e) THIPWM—sinusoid profile: $f_b$=1900 Hz. (f) THIPWM—triangle profile: $f_b$=3700 Hz. (g) SVPWM—constant switching frequency. (h) SVPWM—sinusoid profile: $f_b$=2200 Hz. (i) THIPWM—triangle profile: $f_b$=3700 Hz. Note that only one phase waveforms are recorded.

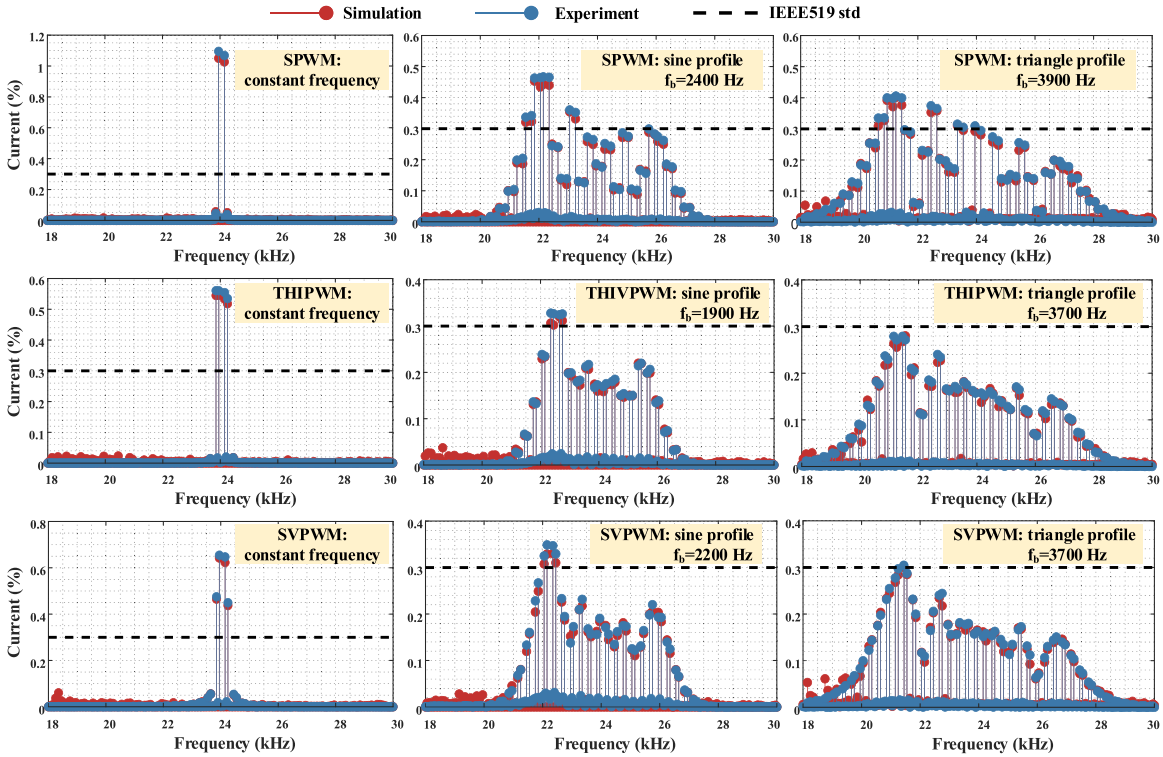


Fig. 16. Grid-side current harmonic spectrum of the first carrier frequency side-bands, derived from the experimental and simulation results.

various PWM methods. The current ripples in the converter-side inductors are significantly attenuated by the adopted *LCL* filter and the grid-side current $i_{\mathrm{g}}$ exhibits good sinusoidal waveform with low THD. Fig. 15 presents the experimental results of the three-phase, two-level inverter under the designed switching profiles. The experimental converter output phase voltage $v_{\mathrm{c}}$, the converter-side current $i_{\mathrm{c}}$, the grid-side current $i_{\mathrm{g}}$, and the ac voltage $v_{\mathrm{ac}}$ match well with the simulation results in terms of waveforms and values. From the results, it can be seen that the switching harmonics in the currents are significantly attenuated by the adopted *LCL* filter. However, in order to validate the effectiveness of the implemented filter and switching profiles, the grid-side current spectra are required for further analysis. By extracting the data of the grid-side currents from both the simulation and experiment results, their corresponding spectra are obtained and subsequently depicted in Fig. 16 in comparison to the limits defined by the current harmonic standard.

First, it can be clearly seen that the two current spectra obtained from the simulation and experimental results match each other with good accuracy under the various PWM methods and switching profiles. The results of the normalized critical current harmonic are summarized in Table III for the intuitive comparison. By comparing the results for different switching profiles with certain modulation method, it is found that the critical current harmonic drops significantly with VSFPWM profiles compared with CSFPWM. Specifically, triangle profile results in the largest reduction (more than 50%) of the critical current harmonic. Besides, a negligible increment of the THD is observed in the grid-side current when the VSFPWM profiles are implemented compared with the relevant CSFPWM.

TABLE III
FILTERING INDUCTANCE REQUIRED BY THE IEEE519 STANDARD

| Switching Profile | $I_{\mathrm{crit}}$ (%) | | THD (%) | Efficiency (%) |
|---|---|---|---|---|
| | Simulation | Experiment | Experimental | Measurement |
| **SPWM** | | | | |
| CSFPWM | 1.05 | 1.07 | 1.14 | 98.00 |
| Sinusoid: $f_b$=2400 Hz | 0.453 | 0.463 | 1.19 | 97.86 |
| Triangle: $f_b$=3900 Hz | 0.402 | 0.408 | 1.19 | 97.80 |
| **1/4 THIPWM** | | | | |
| CSFPWM | 0.545 | 0.560 | 1.00 | 98.00 |
| Sinusoid: $f_b$=1900 Hz | 0.320 | 0.325 | 1.07 | 98.03 |
| Triangle: $f_b$=3700 Hz | 0.267 | 0.280 | 1.06 | 97.94 |
| **SVPWM** | | | | |
| CSFPWM | 0.642 | 0.654 | 1.00 | 98.05 |
| Sinusoid: $f_b$=2200 Hz | 0.33 | 0.345 | 1.04 | 98.02 |
| Triangle: $f_b$=3700 Hz | 0.292 | 0.298 | 1.04 | 98.07 |

Meanwhile, as shown in Table III, the system efficiency also remains nearly unchanged with the implemented VSFPWM profiles.

Additionally, it can be noted that the 1/4 THIPWM method has the overall best current harmonic performance compared with SPWM and SVPWM, when the same filter and switching profile are used. More specifically, the 1/4 THIPWM with the triangle profile ($f_{\mathrm{b}}$) shows the minimum critical current harmonic compared with the rest switching profiles under the same *LCL* filter. In other words, 1/4 THIPWM demands the minimum

inductance for the *LCL* filter to achieve the same current harmonic performance. Therefore, the 1/4 THIPWM with triangle switching profile is regarded as the optimal design choice for the implemented system. Besides, it can be seen that the experimental critical current harmonic values are slightly larger than the simulation ones for all the switching profiles. This implies that the total inductance of the *LCL* filter used in experiment is slightly smaller than 730 $\mu$H. This small difference is acceptable considering the possible variation of core permeability with the current bias during the practical implementation of the *LCL* filter. Therefore, it can be concluded that the VSFPWM following the suggested *LCL* filter design guideline developed in Section III does not substantially influence the THD and efficiency of the system while remarkably lowering the critical harmonic of the grid-side current.

## V. Conclusion

This article has proposed a generic voltage spectrum model for the periodic variable switching frequency modulations in a three-phase, three-wire, two-level VSC. A practical algorithm has also been proposed to make the spectrum calculation feasible. Besides, this article also presents a novel algorithm to find the optimal periodic profiles, which leads to the minimum required inductance for the *LCL* filter while meeting the IEEE519 current harmonic standard. Based on such an algorithm, an *LCL* filter design guideline was devised. Herein, typical periodic variable frequency waveform profiles, such as triangle and sinusoid were studied and implemented. The correctness and feasibility of the proposed periodic VSFPWM spectrum model and their implementation were verified by both simulation and experimental results. The results show that the current THD of the grid-side connection and system efficiency will not be influenced by the VSFPWM under the same ac filter while the critical harmonic is reduced substantially. The optimal periodic switching profiles can lead to a 50% reduction of the required filter inductance compared to the CSFPWM under various PWM methods, implying a significantly reduced filter size and increased power density. Besides, for the specified converter system, the 1/4 THIPWM with a specific triangle switching profile requires the minimal inductance compared with the other studied profiles.

## References


[1] K. Jalili and S. Bernet, "Design of $LC1L$ filters of active-front-end two-level voltage-source converters," *IEEE Trans. Ind. Electron.*, vol. 56, no. 5, pp. 1674–1689, May 2009.

[2] S. Hoffmann, E. Hoene, O. Zeiter, K.-D. Lang, and G. Feix, "Reducing inductor size in high frequency grid feeding inverters," in *Proc. PCIM Europe, Int. Exhib. Conf. Power Electron., Intell. Motion, Renewable Energy Energy Manage.*, 2015, pp. 1–8.

[3] B. Zaidi, A. Videt, and N. Idir, "Optimization method of CM inductor volume taking into account the magnetic core saturation issues," *IEEE Trans. Power Electron.*, vol. 34, no. 5, pp. 4279–4291, May 2019.

[4] K. Park, P. Klaus, and R. M. Burkart, "Spread spectrum modulation for LCL filter design," in *Proc. 20th Int. Symp. Power Electron.*, 2019, pp. 1–6.

[5] Z. Quan, Y. W. Li, and C. Jiang, "Design of interleaved converters with minimum filtering requirement," in *Proc IEEE Appl. Power Electron. Conf. Expo.*, 2019, pp. 404–411.

[6] M. Schweizer, T. Friedli, and J. W. Kolar, "Comparative evaluation of advanced three-phase three-level inverter/converter topologies against two-level systems," *IEEE Trans. Ind. Electron.*, vol. 60, no. 12, pp. 5515–5527, Dec. 2013.

[7] M. Malinowski, K. Gopakumar, J. Rodriguez, and M. Perez, "A survey on cascaded multilevel inverters," *IEEE Trans. Ind. Electron.*, vol. 57, no. 7, pp. 2197–2206, Jul. 2010.

[8] J. Xu, J. Han, Y. Wang, S. Habib, and H. Tang, "A novel scalar PWM method to reduce leakage current in three-phase two-level transformerless grid-connected VSIs," *IEEE Trans. Ind. Electron.*, vol. 67, no. 5, pp. 3788–3797, May 2020.

[9] J. Xu, J. Han, Y. Wang, M. Ali, and H. Tang, "High-frequency SiC three-phase VSIs with common-mode voltage reduction and improved performance using novel tri-state PWM method," *IEEE Trans. Power Electron.*, vol. 34, no. 2, pp. 1809–1822, Feb. 2019.

[10] S. Kaboli, J. Mahdavi, and A. Agah, "Application of random PWM technique for reducing the conducted electromagnetic emissions in active filters," *IEEE Trans. Ind. Electron.*, vol. 54, no. 4, pp. 2333–2343, Aug. 2007.

[11] A. C. B. Kumar and G. Narayanan, "Variable-switching frequency PWM technique for induction motor drive to spread acoustic noise spectrum with reduced current ripple," *IEEE Trans. Ind. Appl.*, vol. 52, no. 5, pp. 3927–3938, Dec. 2016.

[12] D. Jiang and F. Wang, "A general current ripple prediction method for the multiphase voltage source converter," *IEEE Trans. Power Electron.*, vol. 29, no. 6, pp. 2643–2648, Jun. 2014.

[13] X. Mao, R. Ayyanar, and H. K. Krishnamurthy, "Optimal variable switching frequency scheme for reducing switching loss in single-phase inverters based on time-domain ripple analysis," *IEEE Trans. Power Electron.*, vol. 24, no. 4, pp. 991–1001, Apr. 2009.

[14] D. Jiang and F. Wang, "Variable switching frequency PWM for three-phase converters based on current ripple prediction," *IEEE Trans. Power Electron.*, vol. 28, no. 11, pp. 4951–4961, Nov. 2013.

[15] O. Oñederra, I. Kortabarria, I. M. de Alegría, J. Andreu, and J. I. Gárate, "Three-phase VSI optimal switching loss reduction using variable switching frequency," *IEEE Trans. Power Electron.*, vol. 32, no. 8, pp. 6570–6576, Aug. 2017.

[16] Q. Li, J. Chen, and D. Jiang, "Periodic variation in the effect of switching frequency on the harmonics of power electronic converters," *Chin. J. Elect. Eng.*, vol. 6, no. 3, pp. 35–45, Sep. 2020.

[17] D. Gonzalez *et al.*, "Conducted EMI reduction in power converters by means of periodic switching frequency modulation," *IEEE Trans. Power Electron.*, vol. 22, no. 6, pp. 2271–2281, Nov. 2007.

[18] J. Balcells, A. Santolaria, A. Orlandi, D. Gonzalez, and J. Gago, "EMI reduction in switched power converters using frequency modulation techniques," *IEEE Trans. Electromagn. Compat.*, vol. 47, no. 3, pp. 569–576, Aug. 2005.

[19] K. Tse, H. S.-H. Chung, S. Ron Hui, and H. So, "A comparative study of carrier-frequency modulation techniques for conducted EMI suppression in PWM converters," *IEEE Trans. Ind. Electron.*, vol. 49, no. 3, pp. 618–627, Jun. 2002.

[20] G. Holmes, T. Lipo, and T. Lipo, *Pulse Width Modulation for Power Converters: Principles and Practice*. Piscataway, NJ, USA: IEEE Press, 2003.

[21] J. Chen, D. Sha, J. Zhang, and X. Liao, "An SiC MOSFET based three-phase ZVS inverter employing variable switching frequency space vector PWM control," *IEEE Trans. Power Electron.*, vol. 34, no. 7, pp. 6320–6331, Jul. 2019.

[22] J. Chen, D. Sha, J. Zhang, and X. Liao, "A variable switching frequency space vector modulation technique for zero-voltage switching in two parallel interleaved three-phase inverters," *IEEE Trans. Power Electron.*, vol. 34, no. 7, pp. 6388–6398, Jul. 2019.

[23] H. A. Attia, T. K. S. Freddy, H. S. Che, W. P. Hew, and A. H. El Khateb, "Confined band variable switching frequency pulse width modulation (CB-VSF PWM) for a single-phase inverter with an LCL filter," *IEEE Trans. Power Electron.*, vol. 32, no. 11, pp. 8593–8605, Nov. 2017.

[24] D. Holmes, "The significance of zero space vector placement for carrier-based PWM schemes," *IEEE Trans. Ind. Appl.*, vol. 32, no. 5, pp. 1122–1129, Sep./Oct. 1996.

[25] A. Trzynadlowski and S. Legowski, "Minimum-loss vector PWM strategy for three-phase inverters," *IEEE Trans. Power Electron.*, vol. 9, no. 1, pp. 26–34, Jan. 1994.

[26] R. Peña-Alzola, M. Liserre, F. Blaabjerg, M. Ordonez, and Y. Yang, "*LCL* filter design for robust active damping in grid-connected converters," *IEEE Trans. Ind. Informat.*, vol. 10, no. 4, pp. 2192–2203, Nov. 2014.

[27] A. Reznik, M. G. Simões, A. Al-Durra, and S. M. Muyeen, "*LCL* filter design and performance analysis for grid-interconnected systems," *IEEE Trans. Ind. Appl.*, vol. 50, no. 2, pp. 1225–1232, Mar./Apr. 2014.
[28] T.-F. Wu, M. Misra, L.-C. Lin, and C.-W. Hsu, "An improved resonant frequency based systematic LCL filter design method for grid-connected inverter," *IEEE Trans. Ind. Electron.*, vol. 64, no. 8, pp. 6412–6421, Aug. 2017.
[29] S. G. Parker, B. P. McGrath, and D. G. Holmes, "Regions of active damping control for LCL filters," in *Proc. IEEE Energy Convers. Congr. Expo.*, 2012, pp. 53–60.
[30] Y. Tang, W. Yao, P. C. Loh, and F. Blaabjerg, "Design of LCL-filters with LCL resonance frequencies beyond the Nyquist frequency for grid-connected inverters," in *Proc. IEEE Energy Convers. Congr. Expo.*, 2015, pp. 5137–5144.
[31] Y. Tang, C. Yoon, R. Zhu, and F. Blaabjerg, "Generalized stability regions of current control for LCL-filtered grid-connected converters without passive or active damping," in *Proc. IEEE Energy Convers. Congr. Expo.*, 2015, pp. 2040–2047.
[32] J. Wang, J. D. Yan, L. Jiang, and J. Zou, "Delay-dependent stability of single-loop controlled grid-connected inverters with LCL filters," *IEEE Trans. Power Electron.*, vol. 31, no. 1, pp. 743–757, Jan. 2016.
[33] M. Stecca, T. B. Soeiro, L. R. Elizondo, P. Bauer, and P. Palensky, "Comparison of two and three-level DC–AC converters for a 100 kW battery energy storage system," in *Proc. IEEE 29th Int. Symp. Ind. Electron.*, 2020, pp. 677–682.

**Yang Wu** (Student Member, IEEE) received the B.S. degree in electrical engineering and automation, in 2017, from Southeast University, Nanjing, China, and the M.Sc. (*cum laude*) degree in electrical power engineering, in 2019, from the Delft University of Technology, Delft, The Netherlands, where he is currently working toward the Ph.D. degree in electrical engineering with DCES Group (dc systems, energy conversion, and storage).

His research interests include the PWM and control strategies of the grid-connected converter for the EV fast charger.

**Junzhong Xu** (Member, IEEE) was born in Ningbo, China, in 1994. He received the B.S. degree from the Harbin Institute of Technology, Harbin, China, and the Ph.D. degree from Shanghai Jiao Tong University, Shanghai, China, in 2016 and 2021, respectively, both in electrical engineering.

From January 2020 to June 2021, he was a Visiting Scholar with the DC Systems, Energy Conversion and Storage Group, Delft University of Technology, Delft, The Netherlands. He is currently a Postdoctoral Research Fellow with the Department of Electrical Engineering, Shanghai Jiao Tong University, Shanghai, China. His research interests include advanced control and modulation for power converters.

**Thiago Batista Soeiro** (Senior Member, IEEE) received the B.S.(Hons.) and M.S. degrees in electrical engineering from the Federal University of Santa Catarina, Florianopolis, Brazil, in 2004 and 2007, respectively, and the Ph.D. degree from the Swiss Federal Institute of Technology, Zurich, Switzerland, in 2012.

He was a Visiting Scholar with Power Electronics and Energy Research Group, Concordia University, Montreal, QC, Canada, and the Center for Power Electronics Systems, Blacksburg, VA, USA. From 2012 to 2013, he was a Senior Engineer with Power Electronics Institute, the Federal University of Santa Catarina. From 2013 to 2018, he was a Senior Scientist with Corporate Research Center, ABB Switzerland Ltd. From 2018 to 2021, he was with the DC Systems, Energy Conversion and Storage Group, Delft University of Technology, Delft, The Netherlands, where he successfully acquired his Tenure academic position and worked as an Associate Professor for high-power electronics. Since January 2022, he has been with the European Space Agency, European Space Research and Technology Centre, Noordwijk, The Netherlands, where he works on the R&D of power conditioning and distribution units for satellites.

**Marco Stecca** (Student Member, IEEE) received the bachelor's degree in energy engineering from the University of Padova, Padova, Italy, in 2016, and the master's degree in electrical engineering from Politecnico di Milano, Milan, Italy, in 2018. He is currently working toward the Ph.D. degree in grid-scale battery energy storage systems with the Delft University of Technology, Delft, The Netherlands.

His research interests include grid-connected dc–ac power electronics converters and energy storage system integration in distribution grids.

**Pavol Bauer** (Senior Member, IEEE) received the master's degree in electrical engineering from the Technical University of Kosice, Kosice, Slovakia, in 1985, and the Ph.D. degree from the Delft University of Technology, Delft, The Netherlands, in 1995.

He is currently a Full Professor with the Department of Electrical Sustainable Energy, Delft University of Technology, where he is the Head of DC Systems, Energy Conversion and Storage Group. He has authored or co-authored 72 journals and almost 300 conference papers (with H factor Google scholar 43, Web of Science 20) and 8 books, and holds 4 international patents. He has organized several tutorials at the international conferences. He has worked on many projects for industry concerning wind and wave energy, power electronic applications for power systems such as Smarttrafo; HVdc systems, projects for smart cities such as PV charging of electric vehicles, PV and storage integration, contactless charging; and he has participated in several Leonardo da Vinci and H2020 EU projects as project partner (ELINA, INETELE, E-Pragmatic) and coordinator (PEMCWebLab.com-Edipe, SustEner, Eranet DCMICRO).

Dr. Bauer was a recipient of the title Prof. from the President of Czech Republic at the Brno University of Technology in 2008 and the Delft University of Technology in 2016.